

Microstructure formation in micron-scale thin-walled Hastelloy X samples fabricated with laser powder bed fusion

Journal Article**Author(s):**

Wróbel, Rafał; [Scheel, Pooriya](#) ; Maeder, Xavier; Hosseini, Ehsan; Leinenbach, Christian

Publication date:

2024-04

Permanent link:

<https://doi.org/10.3929/ethz-b-000615760>

Rights / license:


[Creative Commons Attribution 4.0 International](#)

Originally published in:

Progress in Additive Manufacturing 9(2), <https://doi.org/10.1007/s40964-023-00458-z>



Microstructure formation in micron-scale thin-walled Hastelloy X samples fabricated with laser powder bed fusion

R. Wróbel^{1,2} · P. Scheel^{1,3} · X. Maeder⁴ · E. Hosseini^{1,3} · C. Leinenbach^{1,5} 

Received: 17 February 2023 / Accepted: 13 May 2023 / Published online: 23 May 2023
© The Author(s) 2023

Abstract

Laser powder bed fusion (LPBF) has great potential for the fabricating complex geometries with improved functionality. In combination with nickel alloys such as Hastelloy X, parts produced with this technology find usage in high-temperature applications. Many studies have focused on the microstructure of Hastelloy X fabricated via LPBF technology, but most have been performed on simple cubic geometries. Considering the aforementioned applications, the parts are often characterized by fine features, like very thin-walled structured, often in the sub-1 mm range. However, little is known about the LPBF fabrication of such structures. The study presented in this paper shows that wall thickness plays an important role in microstructure formation. In situ temperature measurements and thermal simulations showed a difference in thermal history. Local heat accumulation in the vicinity of the scanned tracks was observed for the sample consisting of multiple tracks. Moreover, this effect was enhanced with the number of tracks, leading to different melt pool morphologies. Significantly, coarser solidification cells were found near the sample edges. In addition, larger grains oriented parallel to the build direction were observed for the samples consisting of 3 and more tracks, while for the thinner samples, a very fine microstructure with random orientation was found.

Keywords Laser powder bed fusion · Hastelloy X · Thin-walls · Additive manufacturing

1 Introduction

Metal additive manufacturing (MAM) technologies offer new possibilities for the fabrication of parts with geometries that were impossible to produce in the past. Moreover, due to MAM's vast design freedom, components with new

functionalities can be produced. Laser powder bed fusion (LPBF) is one of the MAM technologies, which offers very high efficiency, high accuracy and is capable of fabricating parts with intricate geometries [1, 2]. In recent years, the applicability of LPBF for the fabrication of complex components (e.g., fuel nozzles, turbine blades) for gas turbines and jet engines has been widely studied [3, 4]. It has been shown that fabricating parts with, e.g., internal cooling channels or lattice-based structures can improve the efficiency or decrease the weight of the component for the forenamed applications, making them also more sustainable [4–6]. Given the conditions under which such parts must operate, like elevated temperatures, these parts are mostly fabricated from solid-solution strengthened nickel-based superalloys. Among the most popular alloys in this group are alloys such as Inconel 718 or Hastelloy X, which offer excellent material properties at elevated temperatures [7]. Moreover, these alloys have good laser processability, in contrast to, for example, precipitate strengthened nickel-base superalloys, which are susceptible to cracking during the MAM process [7].

✉ C. Leinenbach
christian.leinenbach@empa.ch

¹ Empa Swiss Federal Laboratories for Materials Science & Technology, Überlandstrasse 129, 8600 Dübendorf, Switzerland

² Laboratory for Nanometallurgy, Department of Materials, ETH Zürich, Vladimir-Prelog-Weg 1-5/10, 8093 Zurich, Switzerland

³ Department of Mechanical and Process Engineering, Institute for Mechanical Systems, ETH Zürich, Zurich, Switzerland

⁴ Empa Swiss Federal Laboratories for Materials Science & Technology, Feuerwerkstrasse 39, 3603 Thun, Switzerland

⁵ Laboratory for Photonic Materials and Characterization, École Polytechnique Fédérale de Lausanne, 1015 Lausanne, Switzerland

Numerous studies have focused on the microstructure formation of solid-solution strengthened nickel alloys fabricated via LPBF. These alloys exhibit a very similar microstructure consisting of columnar and cellular dendrites in the as-built state [8–11]. However, many studies showed that different process parameters significantly influence grain size and crystallographic orientation. Montero-Sistiaga et al. studied the effect of laser power on the microstructure formation of Hastelloy X [12]. They showed that using high power laser with a top-hat profile and a larger spot size results in larger cell and grain formation with a more pronounced texture. Due to the grain coarsening, the hardness and yield strength decreased. The effect of scanning strategy on the microstructure formation and mechanical properties of Hastelloy X has been studied by Esmailizadeh et al. [13]. It has been shown that increasing the scanning speed resulted in a smaller melt pool and grain refinement, leading to better mechanical performance. Keshavarzkermani et al. have shown that rotating a bi-directional scan pattern 67° per layer leads to grain refinement in LPBF of Hastelloy X compared to the same scan strategy without the rotation [14]. Hibino et al. have shown that by varying parameters such as scanning speed and laser power, different crystallographic textures can be obtained, from monocrystalline (SCM) to crystallographic lamellar (CLM) or polycrystalline microstructure (PCM) [15].

As shown in the previous paragraph, the various process parameters of the LPBF process influence the formation of the microstructure and, consequently, the mechanical properties of the parts produced using this technology. However, nearly all the studies have been carried out on simple cubic geometries, usually in the centimeter length scale. Given the application of the nickel alloys mentioned above, many parts often contain fine features with a thickness of less than 1 mm. This raises the question of whether such thin-walled features exhibit the same microstructures as the bulk cubes.

One of the main differences between thin-walled samples and bulk samples is the area ratio of melt pool to the surrounding powder bed. During the LPBF process, most of the heat is dissipated through the already solidified material and only a minor amount to the powder surrounding the consolidated material. According to Zhang et al., the thermal conductivity of Inconel 625 powder ranges only from 4.9 to 6.2% of their bulk thermal conductivity [16]. Moreover, more laser scans are required during the fabrication of thicker walls, which in turn introduces more heat into the manufactured parts. Finally, to enable fully dense parts, the subsequent tracks need to overlap, which makes a difference for the single-track walls without overlaps. All these factors influence the thermal conditions, impacting the melt pool size, Marangoni convection, and surface tension, ultimately affecting the microstructure formation and the final quality of the part.

Up until now, only a limited number of studies focusing on the effect of different wall thicknesses on the microstructure formation during LPBF are available. Antonysamy et al. investigated the influence of wall thicknesses from 1 to 5 mm, manufactured from Ti-6Al-4V, using selective electron beam melting. They have observed that grains grow inwards from both wall surfaces in a single-track wall with a thickness of 1 mm, whereas in the case of thicker walls, huge elongated grains oriented parallel to the build direction begin to form [17].

A study on the microstructure formation in single-track walls from Inconel 718 fabricated by LPBF in keyhole and conduction mode was carried out by Yang et al. For the samples fabricated in the keyhole mode, differences in the dendrite size at the component's top in comparison to the bottom were noticed. Moreover, a significant difference in the texture between marginal and central zones of the walls have been reported. In addition, formation of γ'/γ'' precipitates in the central zone, under the keyhole mode was observed, which was attributed to the higher cooling rate [18].

Leicht et al. showed pronounced differences in the microstructure of samples with different wall thicknesses between 0.2 and 3.0 mm fabricated from 316L stainless steel by LPBF. Below 0.6 mm wall thickness, small grains inclined towards the samples' center with random orientations were observed. It was explained that smaller grains nucleate from adjacent powder particles to grow towards the center of the wall according to the maximum temperature gradient. For the thicker parts (>0.6 mm), large elongated grains with a pronounced $\langle 101 \rangle$ texture were observed in the center of the sample adjacent to smaller grains inclined to the center of the melt pool. The difference in microstructure disappeared at a thickness of more than 1 mm thickness and only large elongated grains were observed [19].

The work of Yu et al. focused on the influence of different wall thicknesses, ranging from 1 to 4 mm, on the microstructure and mechanical properties of Hastelloy X samples fabricated by LPBF. According to this study, there is no evidence of microstructural differences between the inner part of the wall and the area near the surface. However, a clear textural transition between the thicker part and the thinner part can be seen. A strong $\langle 011 \rangle$ texture was observed in the 4 mm wall, whereas a $\langle 001 \rangle$ texture formed in the build direction for wall thicknesses between 1 and 2 mm [20].

LPBF of thin-walled structures with feature sizes as small as only a few melt tracks and wall thicknesses below 1 mm has not been well studied so far. In particular, information on how the wall thickness influences the thermal history and the microstructure formation in such parts is yet to be available. It is crucial in the further development of the LPBF process to understand any geometry and dimension-related aspects. Therefore, the present study aims to investigate how the thickness influences the microstructure formation of

thin-walled samples (< 1 mm) fabricated from the Ni-based alloy Hastelloy X by LPBF.

2 Materials and methods

2.1 Materials

In this study, a gas-atomized Hastelloy X powder was used as the material feedstock. The powder was provided by Oerlikon AM with a mean diameter (d_{50}) of 32.2 μm . The morphology of the powder is shown in Fig. 1a.

Different sets of thin-walled samples were fabricated using a Sisma MySint 100 (Sisma S.p.A., Italy) LPBF machine. The machine was equipped with a 200 W, 1061 nm fiber laser operating in continuous wave mode with a Gaussian intensity distribution and a 55 μm spot size.

To investigate the influence of the wall thickness on the microstructure formation, a set of samples consisting of walls with a thickness of 1 to 9 tracks and a height of 6 mm were fabricated. All the thin-walled samples were fabricated using parameters that were previously optimized on simple-cubic geometries ($10 \times 10 \times 10 \text{ mm}^3$), resulting in nearly 100% relative density. The parameters were as follows—125 W laser power, 700 mm scanning speed, 0.07 mm hatch spacing, and 0.03 mm layer thickness.

For all samples, a bidirectional scanning strategy was applied as shown at Fig. 1b. The fabricated samples used for the study are shown at Fig. 1c.

2.2 Microstructure characterization

To investigate the microstructure, the samples were prepared according to metallographic standards, including grinding with SiC paper and polishing with silica suspension (6 μm , 3 μm , and 1 μm). In the final step, alumina suspension 0.5 μm was used. The samples were electrochemically

etched in 10% oxalic acid for 10 s at 6 V DC to reveal the microstructure and melt pool boundaries.

Examination of the microstructure was carried out using a Zeiss Axiovert 100 optical microscope, and FEI Nova NanoSEM scanning electron microscope (SEM). Grain orientation and texture were investigated using a TESCAM MIRA scanning electron microscope (SEM) equipped with an electron backscattered diffraction (EBSD) EDAX DigiView V camera. An acceleration voltage of 20 kV, a beam current of 10,000 pA, and 1 μm step size at 15 mm working distance were applied to acquire the EBSD data.

The cooling rates in the melt tracks were estimated based on the primary dendrite arm spacing (PDAS) using the following equation (Eq. 1):

$$\text{PDAS} = a \cdot \varepsilon^{-b} \quad (1)$$

where ε corresponds to the cooling rate, a and b are material constants which are the following for nickel alloys, $a \approx 50$, and $b = 1/3$ [21].

2.3 In situ temperature measurements

The far-field temperature evolution during the fabrication of the different walls was measured using K-type thermocouples. In order to carry out this experiment, a 5 mm thick substrate with channels allowing attachment of the thermocouples directly under the printed walls was fabricated on the build plate. The thermocouples were placed at a distance of around 1 mm from the top surface onto which the thin walls were printed. During each experiment, only 4 walls with different thicknesses were printed to minimize the influence of the heat generated during the fabrication of other walls. The samples with the attached thermocouples are shown in Fig. 2. Acquisition of the signal from the thermocouples was carried out at a frequency of 9.6 kHz using a QuantumX MX840B amplifier.

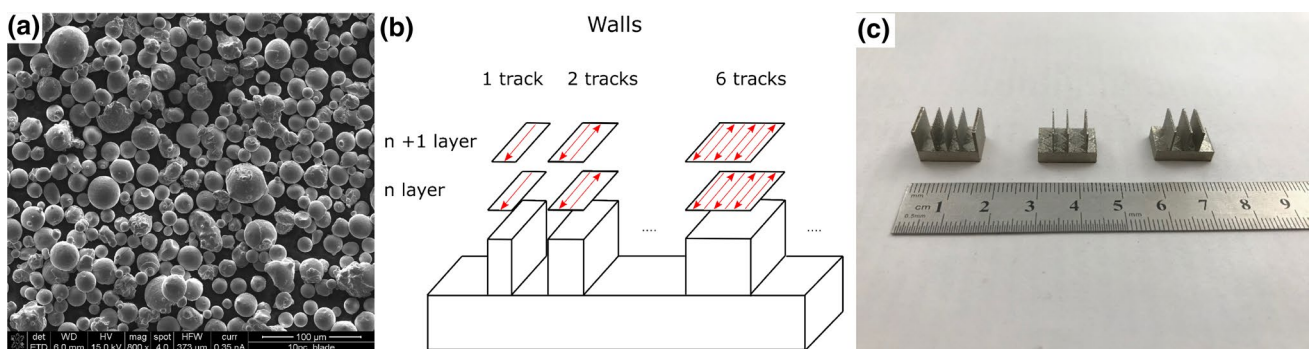
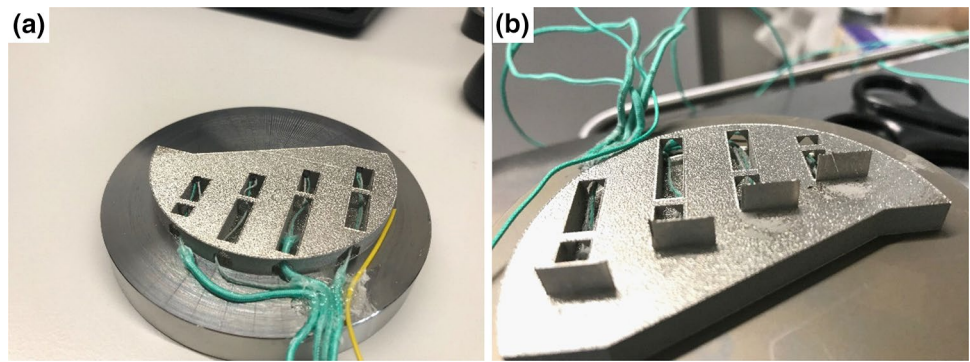


Fig. 1 a Morphology of the Hastelloy X powder used to fabricate the thin-walled samples, b scanning strategy used for the thin-walled-sample fabrication, c fabricated thin-walled samples

Fig. 2 **a** Pre-fabricated substrate with attached thermocouples for in situ temperature measurement of different wall thicknesses, **b** set of fabricated walls with the thermocouples attached underneath



2.4 Thermal model for the simulations

Thermal simulations were performed to study the temperature profiles across different wall thicknesses. The additive manufacturing plugin of the commercially available finite-element software package Abaqus was used to setup the models. Layer deposition was handled using the quiet element approach [22], which means that all deposition layers are present in the model already from the start, but the upper layers are in an inactive state and do not contribute to the solution.

In solving the heat transfer problem, the energy balance equation can be written in the differential form as

$$\rho c_p \dot{T} - \nabla(k \nabla T) = q_{\text{vol}} \quad (2)$$

where T denotes the temperature, ρ , c_p and k are the density, specific heat capacity and thermal conductivity of the materials, respectively. A constant density of 8220 kg/m^3 was used [23] and the temperature-dependent thermal conductivity and specific heat were adopted from [23, 24]. The thermal conductivity at temperatures above the melting point was artificially increased to mimic the increased heat transfer due to liquid convection inside the melt-pool similar to [25]. Furthermore, the latent heat of fusion was implemented as an increase in the specific heat capacity over the melting temperature range.

The right term in Eq. (2), q_{vol} , is the volumetric heat generation from the moving laser. A double ellipsoid Goldak heat source [26] was used to define the laser intensity distribution based on the following equation:

$$q_{\text{vol}} = \eta \frac{6\sqrt{3}f_{f/r}P}{abc_{f/r}\pi\sqrt{\pi}} \exp\left(-\frac{3x^2}{c_{f/r}^2}\right) \exp\left(-\frac{3y^2}{a^2}\right) \exp\left(-\frac{3z^2}{b^2}\right) \quad (3)$$

where η is the absorption coefficient, P is the laser power, and a , b , and c are the ellipsoid parameters. $f_{f/r}$ can be used to determine the fraction of laser energy that is applied in front and rear of the laser ($f_f + f_r = 2$). In this study, a symmetric definition was used, and the ellipsoid parameters were

chosen based on laser spot size ($a = c_{f/r} = \frac{55}{2} \mu\text{m}$) and powder layer thickness ($b = 30 \mu\text{m}$).

At the bottom of the thin walls, a uniform temperature based on the bottom thermocouple readings from in situ measurements was applied as the boundary condition. The combined effect of radiation, convection and conduction to the surrounding powder was represented with a constant film coefficient h_p .

The direct measurement of the parameters η and h_p is challenging in general. As a workaround, the in situ measurements were performed with the thermocouple attached in the middle of the height of the 2-track sample. The collected temperature peaks were used as the basis for calibration of the unknowns, and the resulting values were used to represent all other thicknesses.

3 Results

3.1 Microstructure of thin-walled samples

The microstructures of the samples with different wall thicknesses in the as-built state are presented in Fig. 3. The melt pool contours are clearly visible with respect to the bidirectional scanning strategy that has been applied. A change in the melt pool geometry can be seen for different wall thicknesses, especially for the walls consisting of 1, 2, 3, and 4 tracks (Fig. 3a, d, g, j). For samples thicker than four tracks, no significant differences in their microstructures are observed.

For samples that are only one track wide, the melt pools are relatively shallow and wide, whereas for thicker walls they are more semispherical in the central part of the wall and become shallower on tracks near the edges. Moreover, the solidification cells are larger close to the edges and oriented almost parallel to the build direction. In the single-track sample, two areas within one melt pool can be distinguished—one consisting of very fine solidification cells with sizes up to $0.4 \mu\text{m}$ that have formed at the bottom of the layer

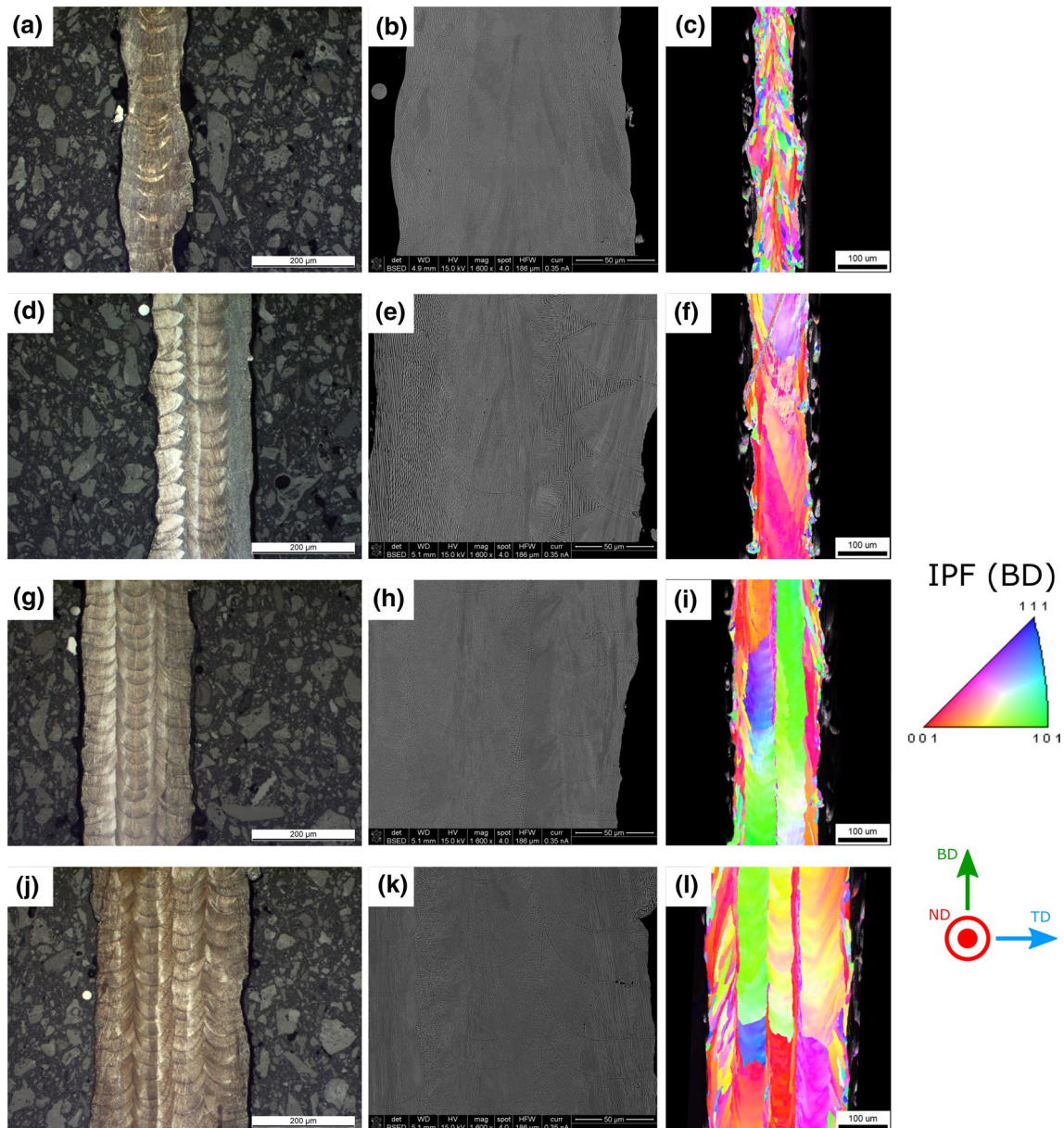


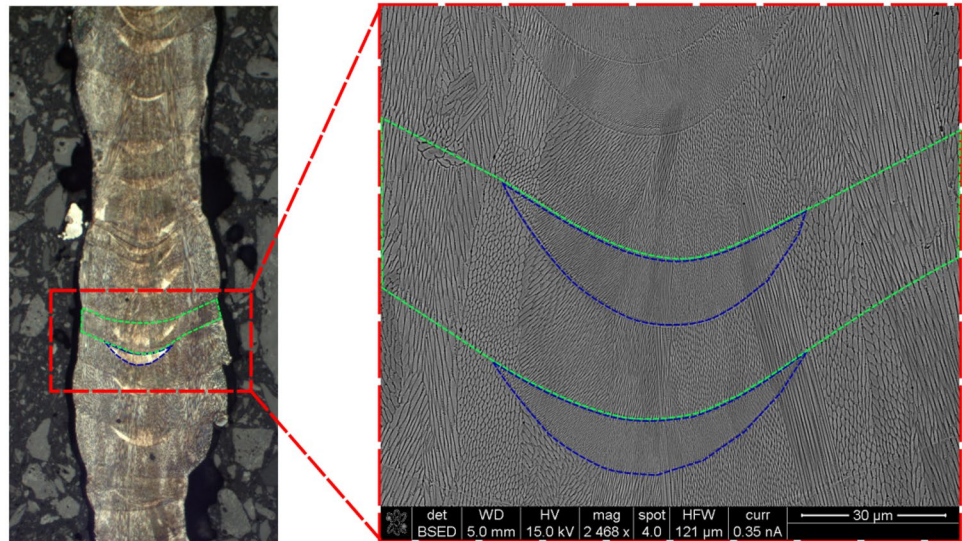
Fig. 3 Microstructure of the **a** OM, **b** SEM, and **c** EBSD for 1-track sample; **d** OM, **e** SEM, and **f** EBSD for 2-track sample; **g** OM, **h** SEM, and **i** EBSD for 3-track sample; **j** OM, **k** SEM, and **l** EBSD for 4-track sample

(Fig. 4—blue color) and another consisting of larger solidification cells up to $0.8 \mu\text{m}$ wide (Fig. 4—green color). The solidification cell size increases progressively between these regions in the centers of the melt pools. According to the PDAS, the estimated cooling rate in the region of very fine solidification cells is approximately $1.9 \times 10^6 \text{ K/s}$, whereas in the second region, the cooling rate is around $3.6 \times 10^5 \text{ K/s}$. The formation of two different zones within one melt pool is not observed in the thicker parts.

The solidification cells in the two tracks wide sample are very fine, in the range of $0.5 \mu\text{m}$, which leads to an estimated cooling rate of $1 \times 10^6 \text{ K/s}$. Moreover, the cells

are directed towards the center of the melt pool. Towards the boundaries of the melt pool, the solidification cells become coarser (Fig. 3e). In addition, coarser and elongated solidification cells oriented parallel to the build direction between the centers of the melt pools appear, reaching up to $1.2 \mu\text{m}$ in width and giving a cooling rate of around $7 \times 10^4 \text{ K/s}$. The microstructure in the thicker samples consisting of more than three tracks (Fig. 3h, k) is very similar to those already reported in the literature [10, 27]. It consists of fine solidification cells that grow epitaxially and parallel to the build direction in the central zone of the melt pool, adjacent to the elongated and

Fig. 4 Microstructure of the melt pool of single-track sample, left OM, right SEM



inclined cells with $\pm 45^\circ$ towards the central zone of the melt pool. In contrast to the microstructure of the double-track sample, the regions between the melt pools consist of coarser solidification cells oriented perpendicular to the build direction (Fig. 3h). When considering the PDAS in the center of each melt pool in every sample, no significant differences nor trends between the subsequently scanned tracks were found. EBSD images are shown in Fig. 3c, f, i, and l for the walls consisting of 1, 2, 3 and 4 tracks, respectively. They show crystallographic orientations with respect to the build direction (IPF BD). In each sample, the grains extend over several layers. For the one track sample, the grains are small compared to the grains observed in the thicker samples. Furthermore, the grains in one track sample are oriented towards the central part of the melt pool, but no pronounced texture is observed. For a sample consisting of two tracks, the grains are inclined in the build direction at an angle of 30° – 40° with a pronounced $\langle 100 \rangle$ orientation, while a fiber texture is observed in the scanning direction. In regions close to the surface, many considerably smaller grains with random texture are noticeable compared to the central part of the sample. In the case of thicker samples, the grains are elongated and oriented parallel to the build direction. They can be longer than $500 \mu\text{m}$ in the build direction. This type of microstructure is similar to the one reported by Montero-Sistiaga et al. for Hastelloy X fabricated with high laser power [12]. In the central part of the sample, a narrow band ($\sim 25 \mu\text{m}$) of grains with a pronounced $\langle 100 \rangle$ orientation is observed. These grains are not present in the melt pools near the edges of the samples. In the case of samples consisting of three or more tracks, rotation of the grains along the $\langle 001 \rangle$ directions can be observed. Starting from

walls consisting of four tracks, this cell rotation effect is disrupted and can no longer be observed.

Figure 5 shows the microstructure of the walls with different thicknesses in their upper part. It can be seen that, for a single-track sample, the top layer of the melt is almost semispherical (Fig. 5a). For the sample consisting of four tracks, it can be observed that in the first track from the left, which was scanned first, the melt pools have a shape that is similar to those observed in the single-track sample. For the subsequent tracks, the melt pools become deeper, and the shapes of the melt pools indicate a change from the conduction mode to the transition mode.

In Fig. 6, inverse pole figures for different wall thicknesses are shown. They have been considered in three directions: $\langle 100 \rangle$, $\langle 010 \rangle$, and $\langle 001 \rangle$, which correspond to the build direction, perpendicular to the scanning direction and nominal to the scanning direction, respectively. Single-track walls do not show a preferred grain orientation in any of the directions. For the sample consisting of two tracks, a fiber texture can be observed in the scanning direction. However, considering the orientation of the grains in the build direction, a transition from $\langle 101 \rangle$ through $\langle 111 \rangle$ to $\langle 100 \rangle$ direction can be observed with the addition of subsequent tracks. For samples that are 4–8 tracks wide, a pronounced texture $\langle 100 \rangle$ is observed in the transverse direction.

3.2 Results from thermocouple measurements

The results of the temperature measurements with the thermocouples for different wall thicknesses are presented in Fig. 7. The signals represent typical temperature–time patterns during LPBF including rapid heating and cooling of the printed parts with the consolidation of every powder layer. Peak temperatures increase as the wall thickness

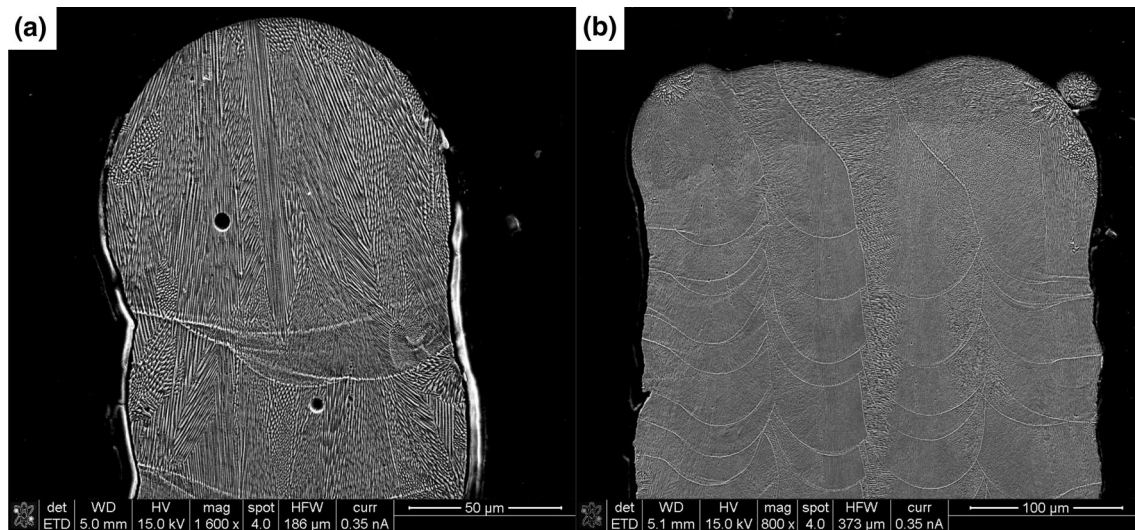


Fig. 5 Microstructure at the top of the wall of the **a** 1 track **b** 4 track

increases. With increasing time, i.e., increasing number of powder layers, the maximum peak temperature decreases as the distance between the bottom of the wall and the scanned layer increases. A certain heat accumulation can be observed for all the samples as the minimum peak temperatures reach a value slightly higher than the ambient temperature. This effect, however, stabilizes after about 850 s (e.g., 150 layers) and the temperature for the very thin-walled samples (1, 2, 3 and 4 tracks) even starts to slightly decrease again, while for the other walls (5, 6, 7 and 8 tracks), it remains almost constant.

3.3 Thermal simulation results

In Fig. 8, the results from the thermal simulations are shown for different wall thicknesses (1–4 tracks). The temperature distribution was captured directly in the center of the sample when the laser was passing by. Moreover, 1300 °C has been chosen as the upper limit of color contours, which corresponds approximately to the melting temperature of Hastelloy X. The regions above this temperature are marked in grey which illustrates the distribution of the molten material.

The local temperature distribution in the vicinity of the melt pool is significantly different in all samples. For the one track sample (Fig. 8a), the area with temperatures above the melting point is significantly larger than that for the thicker samples. However, a similar effect was observed in the case of the thicker samples when the laser was scanning the tracks near the edges of the sample. In walls consisting of more than one track, a pronounced accumulation of heat can be observed. Temperatures in the region adjacent to the scanned track reach values in the range of 600–700 °C. This effect is even more pronounced for the thicker walls, due to

heat accumulation. The area of > 600 °C zone increased in the thicker samples and it is approximately four times larger for the sample consisting of three tracks than for the sample consisting of two tracks, and this trend is also visible for the thicker parts.

4 Discussion

The results indicate significant differences in the microstructures of thin-walled Hastelloy X samples with different wall thicknesses produced by LPBF under the same processing conditions, which were previously optimized for bulk samples. This indicates that the sample dimensions have a pronounced influence on the microstructure formation, in addition to the ‘optimum’ LPBF process parameters such as laser power, scanning speed, hatch spacing, and layer thickness.

4.1 Thermal history simulations and in situ thermocouple measurements

Considering the thermal history of the process, in all samples, after scanning one layer, the temperature as measured with the thermocouple decreases to nearly ambient temperature, indicating that the differences in the temperature gradients do not come from a global preheating of the entire part but it is limited to a certain area.

Taking into account the local temperature distribution in the different parts derived from the simulation results, the most significant difference is observed between the samples consisting of one and two tracks. In the second case, a local preheating of the region adjacent to the scanned track is

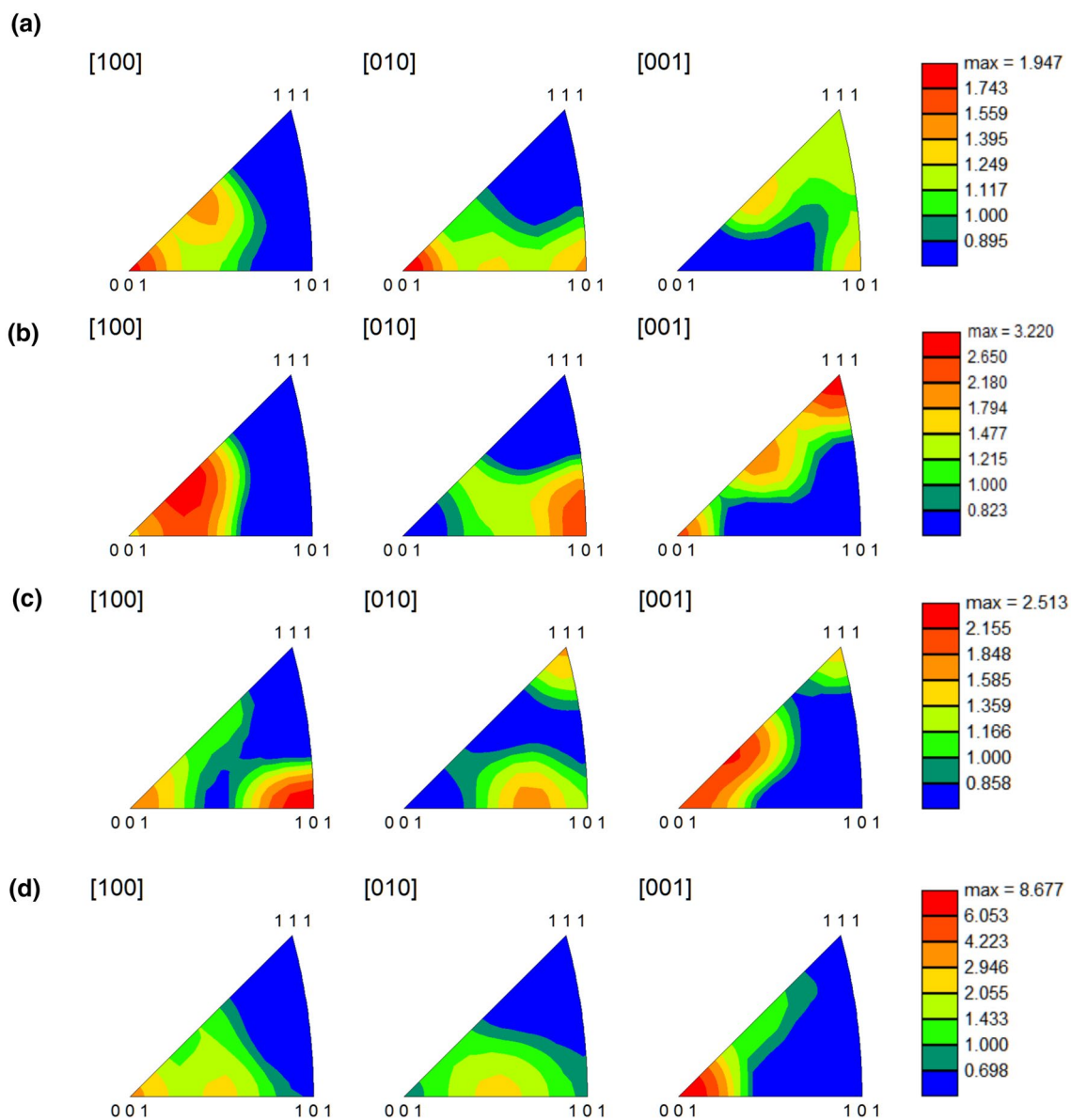


Fig. 6 Inverse pole figures for wall consisting of **a** 1 track, **b** 2 tracks, **c** 3 tracks, and **d** 4 tracks in direction of [100], [010], and [001] corresponding to the build direction, nominal direction, and transverse direction, respectively

observed, where the temperature reaches approximately 700 °C just before the second track is scanned. By increasing the number of tracks, more heat is introduced into the part, leading to a more pronounced local ‘preheating’.

Chen et al. confirmed that preheating causes a much deeper depression zone, due to a higher recoil pressure and stronger evaporation effect resulting in a deeper melt pool [28]. This effect can be also observed in the present case where the local preheating in the samples consisting of three tracks can reach up to 500 °C before the scanning of the subsequent track, while in the single track sample almost no preheating is observed. Thus, the temperature accumulation in the multi-track samples results in the formation of a

deeper melt pool. Moreover, it can be seen from the thermocouple tests that the temperature minima peaks always reaches approximately 30–50 °C for the thinnest and thickest sample, respectively. Thus, the thermocouple tests prove the preheating of the entire part is almost negligible.

4.2 Melt pool size and shape

At the melt pool scale, the most pronounced differences between the different wall thicknesses are observed for samples consisting of one to four tracks (Fig. 3). In the single-track wall, the melt pools are relatively shallow and become even more flattened towards the wall surface.

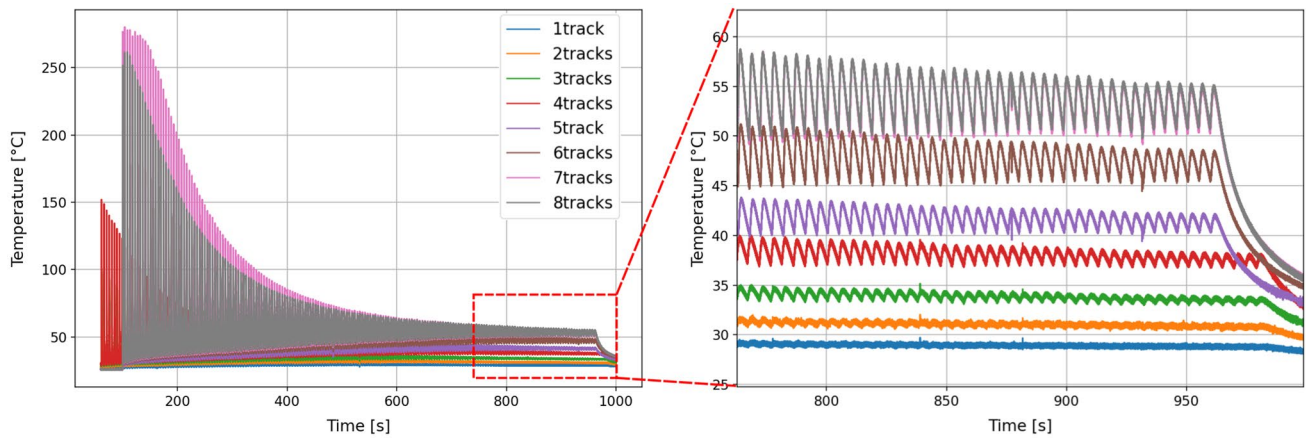


Fig. 7 Temperature profile at the bottom of each wall thickness measured with thermocouples

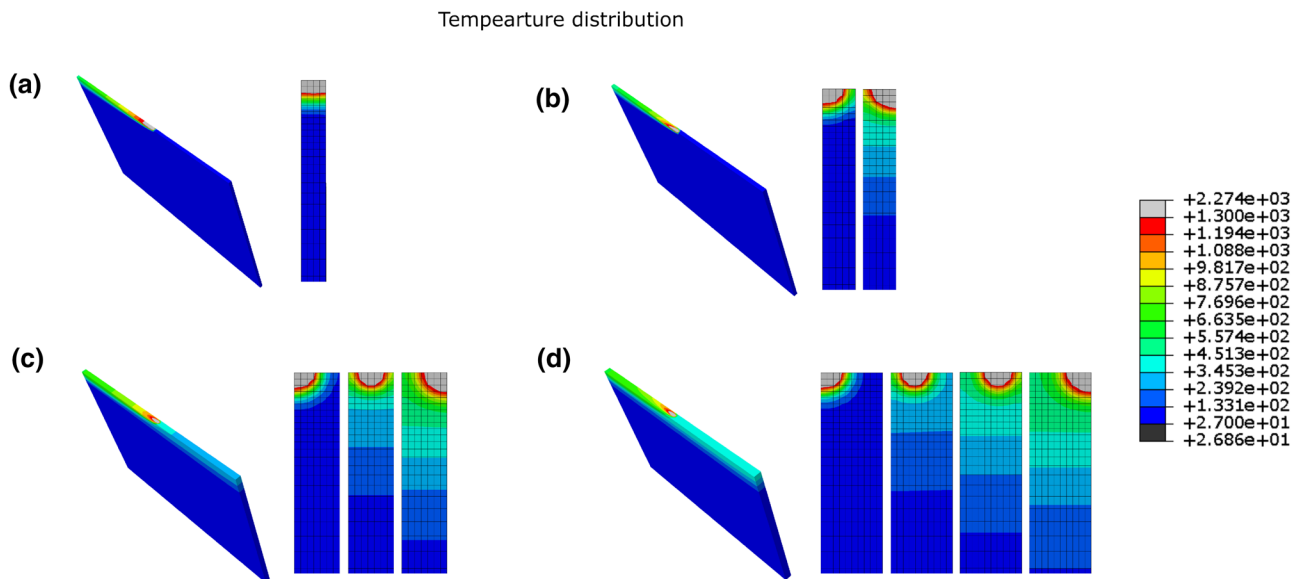


Fig. 8 Thermal simulation results showing the thermal distribution in the middle of the track in the left column and calculated cooling rates in the right column for **a** 1-track, **b** 2-track, **c** 3-track, and **d** 4-track samples

Considering the thermal history, the heat dissipation occurs mainly through the already solidified material, while the heat loss to the powder bed is limited: the heat conductivity of the powder is estimated to 3–5% of the conductivity of the bulk material. Therefore, a pronounced heat accumulation is observed in the vicinity of the melt pool. As a result, the melt pool reaches higher temperatures and the surface tension and viscosity of the melt are reduced. Then, the liquid starts to flow over the powder underneath due to gravitational forces that are acting on the melt in the vicinity of the powder bed, and it flows also to the depression zone in the center of the melt pool that has been created, because of the recoil pressure. Given that no local preheating occurs in the initial phase, the melt pool solidifies very rapidly before the

edge of the melt collapses onto the powder. In the second phase, a relatively high volume of the liquid flows to the depression zone and to the side, onto the powder. The heat cannot be dissipated as rapidly as in the initial step, resulting in lower cooling rates as indicated by larger solidification cells. This is schematically shown in Fig. 9a.

As the wall thickness increases, the melt pools become deeper in the central part of the samples and approach a shape that is indicative of transition mode melting. One of the reasons for this phenomenon is the different temperature gradients that occur during the fabrication of walls with different thicknesses. As has been mentioned in Sect. 4.1, the local preheating in the thicker parts results in a more pronounced depression zone which leads to a deeper melt pool.

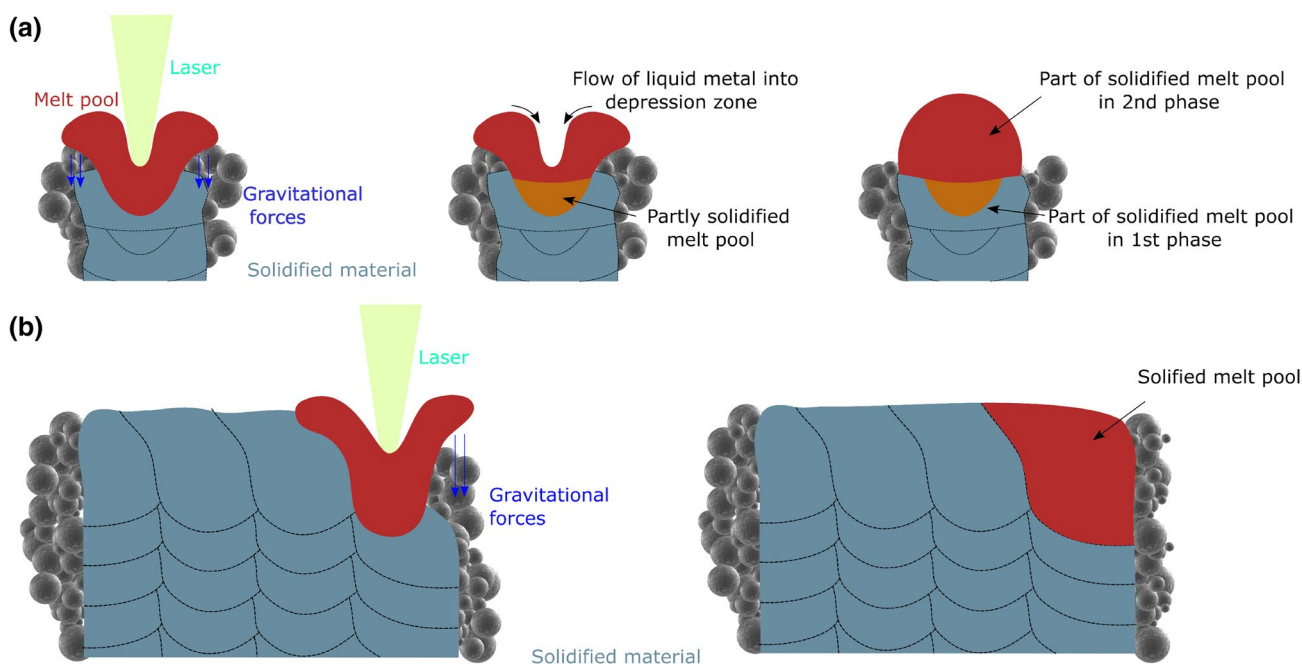


Fig. 9 Formation of the melt pools in **a** 1-track sample, **b** 4-track sample—schematic

In regions near the edges of the thicker walls, the melt pools are shallower and wider, and almost flattened towards the surface. This effect is similar to the one in the single track sample—the heat accumulation observed near the edges of the samples leads to a flow of the liquid over the powder in the vicinity of the melt pool. This effect is shown schematically in Fig. 9b.

Considering the morphology of the top surface of the different wall thicknesses (Fig. 5), it can be seen that the single-track sample shows a rounded geometry. In contrast, the top surfaces of thicker samples are much flatter.

One reason is the difference in the thermal conditions, which affects the wettability of the substrate. In case of the single-track wall, neither local-preheating nor partial remelting of the subsequent track takes place. Therefore, the surface tension of the melt is higher in the single-track sample, which prevents the metal from flowing to the sides, beyond the edge of the walls. Moreover, the area under the scanned track is significantly smaller in contrast to the thicker walls, resulting in a limited area to wet. Thus, the same volume of the liquid metal needs to cover a smaller area, which might also result in the formation of a thicker layer in the thinner walls.

The top surface morphology also has an effect on the powder deposition. A rounded top surface in combination with a thicker solidified layer may lead to an inhomogeneous powder deposition. In this case, the assumed thickness of the new powder layer will differ from the real one. Larger particles will be trapped between the coater and the thin wall and

will not be deposited on the top surface of the wall. Thus, only the smaller powder particles will be deposited on top of the samples. Moreover, larger powder particles that are segregated to the edges of the samples might also be sintered to the wall, which, ultimately will affect the quality of the side surface of the thin wall.

4.3 Microstructure formation

Solidification cell structure In the single-track sample, two regions can be distinguished—very fine solidification cells in the bottom part of the melt pool and, directly above, coarser solidification cells.

As indicated in Fig. 9, solidification occurs in two stages. In the first stage, solidification takes place at the center bottom of the melt pool, due to the direct heat dissipation to the already solidified material, which is larger than the heat dissipation into the powder (Fig. 7a). In the second stage, collapse of the melt pool edges takes place, leading to the flow of the melt not only towards the powder, but also to the central part of the melt pool, where the solidification subsequently takes place. Since a large volume of the liquid metal flows into the central part of the melt pool, the heat dissipation is limited (due to the limited heat loss to the powder and also the heat capacity of the molten material), leading to a lower cooling rate and resulting in the formation of coarser solidification cells.

In the thicker samples, the effect of constrained heat dissipation is visible in the vicinity of the edges of the samples.

The solidification cells are also coarser compared to the central part of the samples. For the thicker samples, the solidification cells in the central part have more or less the same size and no significant variation in the cell size was observed. This indicates that the cooling rate in the central part is similar for all the samples.

Thus, despite a larger volume of solidified material supports heat dissipation in the thicker samples, a local-preheating prevents faster heat dissipation.

In the samples consisting of three and more tracks, large, elongated, columnar solidification cells oriented parallel to the build direction could be observed. They are located in the centers of the melt pools and grow epitaxially across several layers, which has already been reported in numerous studies [15, 29, 30]. These have a $\langle 100 \rangle$ orientation, which is the preferential growth orientation for face-centered cubic materials. The formation of these type of cells usually occurs when the thermal gradient and solid–liquid interface are parallel to the build direction. It should be noted that the largest thermal gradient is normal to the melt pools boundary [31]. Thus, these cells form only in the central part of the walls, where the melt pools become significantly deeper. On the contrary, the cells grow parallel to the build direction in the melt pools near the edges, due to significantly shallower melt pools.

Grain microstructure Considering the EBSD results, the grain size varied significantly between the single-, double-, and triple-track samples. In the single-track samples, fine grains without pronounced texture are observed. The grains are oriented towards the center of the melt pool, which is strongly associated with the solidification direction; solidification starts at the edges of the melt pool and propagates to the central part of the top of the melt pool. Even finer grains were observed closer to the edges of the walls, indicating that solidification also takes place on the powder that is directly fused to the melt pool. As previously mentioned, the melt-pool flows and solidifies over the powder particles, and the random texture is adapted from the powder which determines the formation of the random texture. This phenomenon has also been reported by Leicht et al. [19].

In the sample consisting of two tracks, the grains inclined by $\sim 30^\circ$ to the build direction are observed. This is probably due to the continuation of solidification from the already molten adjacent track, nucleation is facilitated on already solidified grains. This phenomenon is observed in the double-track sample but not in the thicker ones, because in the 2-track samples melt pools are slightly wider and shallower, resulting in a more pronounced overlap in contrast to the thicker samples. In the samples consisting of 3 tracks and more, the grains are coarser, which is a result of the local preheating and the lower cooling rates. Moreover, grains are oriented almost parallel to the build direction, and the orientation changes almost in the middle of each melt pool

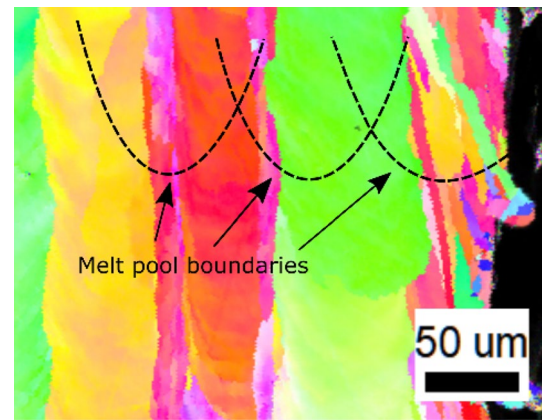


Fig. 10 EBSD images with the contours of the melt pools indicating the areas of the texture transition

(Fig. 10). Thus, a change of orientation occurs when half of the melt pool is remelted during the scanning of the next track. The same type of microstructure has been reported in the literature [15].

5 Conclusion

In this study, the impact of the wall thickness on the microstructure in thin-walled (< 1 mm) Hastelloy X samples produced with LPBF was studied. It has been shown that the wall thickness is an important parameter that should be considered during the design process of the parts and that applying process parameters that were optimized for bulk samples will result in significantly different microstructures in thin-walled samples. The main findings are:

1. The main difference in the microstructure occurs between the samples consisting of one, two and three tracks. The thinnest sample is characterized by very fine grains which tend to be coarser as the number of tracks increases. This difference vanishes for the walls that are larger than three tracks. These consist of large and elongated grains parallel to the build direction with a length exceeding $500 \mu\text{m}$. This has been explained by the difference in the thermal history between these samples. The simulation results and in-situ temperature measurements show local preheating in the vicinity of the melt pools in the thicker samples, resulting in lower thermal gradients.
2. It has been shown that deeper, semi-spherical melt pools form in samples consisting of more than three tracks, which occurs only in the central part of the walls. This led to the formation of solidification cells parallel to the build direction with $\langle 100 \rangle$ orientation.

3. In all of the samples, near the edges, coarser solidification cells were observed, due to the limited heat loss to the powder bed resulting in a lower cooling rate.
4. The smaller grains with random orientation were found near the edges of all the samples. It has been found that partial solidification on the powder particles fused to the walls takes place. The width of this area was estimated to be around 60–80 μm .
5. The single-track samples are characterized by two regions of very fine and coarse solidification cells. It is proposed that solidification takes place in two steps solidification at high cooling in the first stage and in the second lower cooling rate, due to the larger melt flow towards the depression zone of the melt. Moreover, a very fine grain structure was observed with random texture.

Acknowledgements The financial support from the ETH Zurich Foundation through the project no. 2018-HE-321 “Combustion Dynamics Optimisation for LiQuid Fuel firEd Gas Turbines (QUIET)” is gratefully acknowledged.

Author contributions RW: conceptualization, methodology, validation, investigation, data curation, visualization, writing—original draft. PS: validation, methodology, investigation, data curation, writing—review and editing. XM: validation, investigation, writing—review and editing. EH: validation, writing—review and editing. CL: conceptualization, writing—review and editing, project administration, supervision.

Funding Open Access funding provided by Lib4RI – Library for the Research Institutes within the ETH Domain: Eawag, Empa, PSI & WSL.

Data availability The data presented in this work will be made available upon reasonable request.

Declarations

Conflict of interest The authors declare that they have no known competing financial interests or personal relationships that could have appeared to influence the work reported in this paper.

Open Access This article is licensed under a Creative Commons Attribution 4.0 International License, which permits use, sharing, adaptation, distribution and reproduction in any medium or format, as long as you give appropriate credit to the original author(s) and the source, provide a link to the Creative Commons licence, and indicate if changes were made. The images or other third party material in this article are included in the article's Creative Commons licence, unless indicated otherwise in a credit line to the material. If material is not included in the article's Creative Commons licence and your intended use is not permitted by statutory regulation or exceeds the permitted use, you will need to obtain permission directly from the copyright holder. To view a copy of this licence, visit <http://creativecommons.org/licenses/by/4.0/>.

References

1. Martin JH, Yahata BD, Hundley JM et al (2017) 3D printing of high-strength aluminium alloys. *Nature* 549:365–369. <https://doi.org/10.1038/nature23894>
2. Wauthle R, Vrancken B, Beynaerts B et al (2015) Effects of build orientation and heat treatment on the microstructure and mechanical properties of selective laser melted Ti6Al4V lattice structures. *Addit Manuf* 5:77–84. <https://doi.org/10.1016/j.addma.2014.12.008>
3. Ealy B, Calderon L, Wang W et al (2017) Characterization of laser additive manufacturing-fabricated porous superalloys for turbine components. *J Eng Gas Turbines Power* 139:102102. <https://doi.org/10.1115/1.4035560>
4. Bernstein JA, Bravato A, Ealy B, et al (2013) Fabrication and analysis of porous superalloys for turbine components using laser additive manufacturing. In: 49th AIAA/ASME/SAE/ASEE Joint Propulsion Conference. American Institute of Aeronautics and Astronautics, San Jose, CA
5. Liu R, Wang Z, Sparks T, et al (2017) Aerospace applications of laser additive manufacturing. In: *Laser additive manufacturing*. Elsevier, pp 351–371
6. Sanchez S, Smith P, Xu Z et al (2021) Powder Bed Fusion of nickel-based superalloys: a review. *Int J Mach Tools Manuf* 165:103729. <https://doi.org/10.1016/j.ijmactools.2021.103729>
7. Attallah MM, Jennings R, Wang X, Carter LN (2016) Additive manufacturing of Ni-based superalloys: the outstanding issues. *MRS Bull* 41:758–764. <https://doi.org/10.1557/mrs.2016.211>
8. Marchese G, Lorusso M, Parizia S et al (2018) Influence of heat treatments on microstructure evolution and mechanical properties of Inconel 625 processed by laser powder bed fusion. *Mater Sci Eng A* 729:64–75. <https://doi.org/10.1016/j.msea.2018.05.044>
9. Marchese G, Parizia S, Rashidi M et al (2020) The role of texturing and microstructure evolution on the tensile behavior of heat-treated Inconel 625 produced via laser powder bed fusion. *Mater Sci Eng A* 769:138500. <https://doi.org/10.1016/j.msea.2019.138500>
10. Tomus D, Rometsch PA, Heilmaier M, Wu X (2017) Effect of minor alloying elements on crack-formation characteristics of Hastelloy-X manufactured by selective laser melting. *Addit Manuf* 16:65–72. <https://doi.org/10.1016/j.addma.2017.05.006>
11. Yin Y, Zhang J, Gao J et al (2021) Laser powder bed fusion of Ni-based Hastelloy X superalloy: Microstructure, anisotropic mechanical properties and strengthening mechanisms. *Mater Sci Eng A* 827:142076. <https://doi.org/10.1016/j.msea.2021.142076>
12. Montero-Sistiaga ML, Pourbabak S, Van Humbeeck J et al (2019) Microstructure and mechanical properties of Hastelloy X produced by HP-SLM (high power selective laser melting). *Mater Des* 165:107598. <https://doi.org/10.1016/j.matdes.2019.107598>
13. Esmailizadeh R, Keshavarzkermani A, Ali U et al (2020) Customizing mechanical properties of additively manufactured Hastelloy X parts by adjusting laser scanning speed. *J Alloys Compd* 812:152097. <https://doi.org/10.1016/j.jallcom.2019.152097>
14. Keshavarzkermani A, Esmailizadeh R, Ali U et al (2019) Controlling mechanical properties of additively manufactured hastelloy X by altering solidification pattern during laser powder-bed fusion. *Mater Sci Eng A* 762:138081. <https://doi.org/10.1016/j.msea.2019.138081>
15. Hibino S, Todo T, Ishimoto T et al (2021) Control of crystallographic texture and mechanical properties of hastelloy-X via laser powder bed fusion. *Crystals* 11:1064. <https://doi.org/10.3390/cryst11091064>
16. Zhang S, Lane B, Whiting J, Chou K An investigation into metallic powder thermal conductivity in laser powder-bed fusion additive manufacturing 12

17. Antonysamy AA, Meyer J, Prangnell PB (2013) Effect of build geometry on the β -grain structure and texture in additive manufacture of Ti6Al4V by selective electron beam melting. *Mater Charact* 84:153–168. <https://doi.org/10.1016/j.matchar.2013.07.012>
18. Yang H, Yang J, Huang W et al (2018) The printability, microstructure, crystallographic features and microhardness of selective laser melted Inconel 718 thin wall. *Mater Des* 156:407–418. <https://doi.org/10.1016/j.matdes.2018.07.007>
19. Leicht A, Klement U, Hryha E (2018) Effect of build geometry on the microstructural development of 316L parts produced by additive manufacturing. *Mater Charact* 143:137–143. <https://doi.org/10.1016/j.matchar.2018.04.040>
20. Yu C-H, Peng RL, Luzin V et al (2020) Thin-wall effects and anisotropic deformation mechanisms of an additively manufactured Ni-based superalloy. *Addit Manuf* 36:101672. <https://doi.org/10.1016/j.addma.2020.101672>
21. Li S, Wei Q, Shi Y et al (2015) Microstructure characteristics of inconel 625 superalloy manufactured by selective laser melting. *J Mater Sci Technol* 31:946–952. <https://doi.org/10.1016/j.jmst.2014.09.020>
22. SIMULIA User Assistance (2020) Dassault Systemes Simulia Corp, United States, 2020
23. Physical Properties. <https://www.haynesintl.com/alloys/ally-portfolio/High-temperature-Alloys/HASTELLOY-X-alloy/physical-properties>. Accessed 24 Aug 2021
24. Millis KC (2002) Recommended values of thermophysical properties for selected commercial alloys, p. 175-180, Woodhead Publishing Limited, Cambridge
25. Luo Z, Zhao Y (2020) Efficient thermal finite element modeling of selective laser melting of Inconel 718. *Comput Mech* 65:763–787. <https://doi.org/10.1007/s00466-019-01794-0>
26. Goldak J, Chakravarti A, Bibby M (1984) A new finite element model for welding heat sources. *MTB* 15:299–305. <https://doi.org/10.1007/BF02667333>
27. Mertens R (2018) Selective laser melting of aluminum, Hastelloy X, tool steel and cobalt-chrome: compositional modification and use of base plate preheating. PhD thesis Nr 1748825, KU Leuven
28. Chen Q, Zhao Y, Strayer S et al (2021) Elucidating the effect of preheating temperature on melt pool morphology variation in Inconel 718 laser powder bed fusion via simulation and experiment. *Addit Manu* 37:101642. <https://doi.org/10.1016/j.addma.2020.101642>
29. Sun S-H, Hagihara K, Nakano T (2018) Effect of scanning strategy on texture formation in Ni-25at.%Mo alloys fabricated by selective laser melting. *Mater Des* 140:307–316. <https://doi.org/10.1016/j.matdes.2017.11.060>
30. Sun S-H, Ishimoto T, Hagihara K et al (2019) Excellent mechanical and corrosion properties of austenitic stainless steel with a unique crystallographic lamellar microstructure via selective laser melting. *Scripta Mater* 159:89–93. <https://doi.org/10.1016/j.scriptamat.2018.09.017>
31. Thijs L, Verhaeghe F, Craeghs T et al (2010) A study of the microstructural evolution during selective laser melting of Ti–6Al–4V. *Acta Mater* 58:3303–3312. <https://doi.org/10.1016/j.actamat.2010.02.004>

Publisher's Note Springer Nature remains neutral with regard to jurisdictional claims in published maps and institutional affiliations.